

Room Temperature Chiral Coupling of Valley Excitons with Spin-Momentum Locked Surface Plasmons

Thibault Chervy,^{†,‡} Stefano Azzini,^{†,‡} Etienne Lorchat,[§] Shaojun Wang,^{||} Yuri Gorodetski,[⊥] James A. Hutchison,[†] Stéphane Berciaud,^{§,✉} Thomas W. Ebbesen,^{†,✉} and Cyriaque Genet^{*,†,✉}

[†]ISIS and icFRC, Université de Strasbourg and CNRS, UMR 7006, F-67000 Strasbourg, France

[§]Université de Strasbourg, CNRS, IPCMS, UMR 7504, F-67000 Strasbourg, France

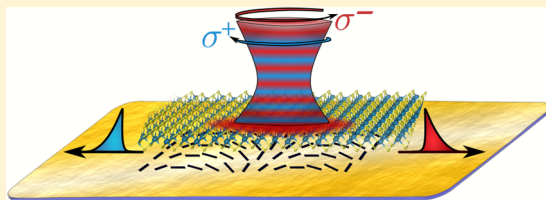
^{||}Dutch Institute for Fundamental Energy Research, Eindhoven, The Netherlands

[⊥]Mechanical Engineering and Mechatronics Department and Electrical Engineering and Electronics Department, Ariel University, Ariel 40700, Israel

Supporting Information

ABSTRACT: We demonstrate room temperature chiral coupling of valley excitons in a transition metal dichalcogenide monolayer with spin-momentum locked surface plasmons. At the onset of the strong coupling regime, we measure spin-selective excitation of directional flows of polaritons. Operating under such conditions, our platform yields surprisingly robust intervalley contrasts (ca. 40%) and coherence (ca. 5–8%) as opposed to their total absence for the uncoupled valley excitons at room temperature. These results open rich possibilities, easy to implement, in the context of chiral optical networks.

KEYWORDS: chiral coupling, transition metal dichalcogenide monolayer, surface plasmons, valley polarization and coherence, optical spin–orbit interaction, plasmonic spin-momentum locking



Optical spin–orbit (OSO) interaction couples the polarization of a light field with its propagation direction.¹ An important body of work has recently described how OSO interactions can be exploited at the level of nano-optical devices, involving dielectric,^{2–5} or plasmonic architectures,^{6–11} all able to confine the electromagnetic field below the optical wavelength. Optical spin-momentum locking effects have been used to spatially route the flow of surface plasmons depending on the spin of the polarization of the excitation beam¹² or to spatially route the flow of photoluminescence (PL) depending on the spin of the polarization of the emitter transition.¹³ Such directional coupling, also known as chiral coupling, has been demonstrated in both classical and quantum regimes.^{14–20} Chiral coupling opens new opportunities in the field of light–matter interactions with the design of nonreciprocal devices, ultrafast optical switches, nondestructive photon detector, and quantum memories and networks (see ref 21 and references therein).

In this letter, we propose a new platform consisting of valley-polarized excitons of a transition metal dichalcogenide (TMD) monolayer coupled to a plasmonic OSO mode, at room temperature (RT). Considering the coupling strengths reached in this system, each spin-polarized valley exciton becomes hybridized with a single plasmon mode of specific momentum. The chiral nature of this interaction generates spin-momentum locked polaritonic states, which we will refer to with the portmanteau chiralitons. A striking feature of our platform is its capacity to induce RT robust valley contrasts, enabling the

directional transport of chiralitons over microscale distances. Interestingly, this coupling regime also yields coherent intervalley dynamics whose contribution can still be observed in the steady-state. We, hence, demonstrate the generation of coherent superpositions (i.e., pairs) of chiralitons flowing in opposite directions. These results, unexpected from the bare TMD monolayer RT properties,^{22–24} point toward the role played by valley-selective chiral coupling as a new mean for protecting the coupled system from valley decoherence.^{25–28}

The small Bohr radii and reduced screening of monolayer TMD excitons provide the extremely large oscillator strength required for light–matter interaction in the strong coupling regime, as already achieved in Fabry–Pérot cavities^{29–31} and more recently in plasmonic resonators.^{32,33} In this context, Tungsten Disulfide (WS₂) naturally sets itself as a perfect material for RT strong coupling³³ due to its sharp and intense A-exciton absorption peak, well separated from the higher energy B-exciton line (see Figure 1a).³⁴ Moreover, the inversion symmetry breaking of the crystalline order on a TMD monolayer, combined with time-reversal symmetry, leads to spin-polarized valley transitions at the K and K' points of the associated Brillouin zone, as sketched in Figure 1b.³⁵ This polarization property makes therefore atomically thin semi-conducting TMDs very promising candidates with respect to the chiral aspect of the coupling between the excitonic valleys

Received: September 10, 2017

Published: January 25, 2018

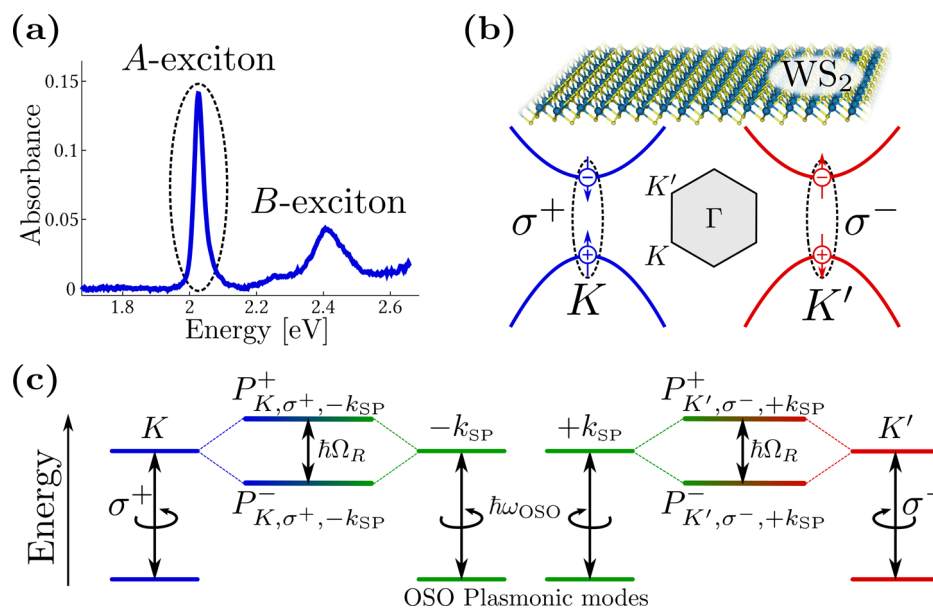


Figure 1. (a) Absorbance spectrum of an exfoliated WS₂ monolayer deposited on a glass substrate, obtained from its transmission spectrum using a broadband incoherent white light source. (b) Crystal packing of a tungsten disulfide (WS₂) monolayer, and sketch of its electronic band structure around the points *K* and *K'* of the Brillouin zone, with the corresponding optical selection rules for band-edge excitons formation under left (σ⁺) and right (σ⁻) circular excitation. (c) Energy level diagram of the *K* and *K'* excitons of WS₂ strongly coupled to an OSO plasmonic mode at energy ħω_{OSO} and wavevector ±k_{SP}.

and the plasmonic OSO modes,^{36,37} resulting in the strongly coupled energy diagram shown in Figure 1c.

Experimentally, our system, shown in Figure 2a, consists of a mechanically exfoliated monolayer of WS₂ covering a plasmonic OSO hole array, with a 5 nm thick dielectric spacer (poly(methyl methacrylate)). The array, imaged in Figure 2b, is designed on a (*x*,*y*) square lattice with a grating period Λ and consists of rectangular nanoapertures (160 × 90 nm²) rotated stepwise along the *x*-axis by an angle $\phi = \pi/6$. The associated

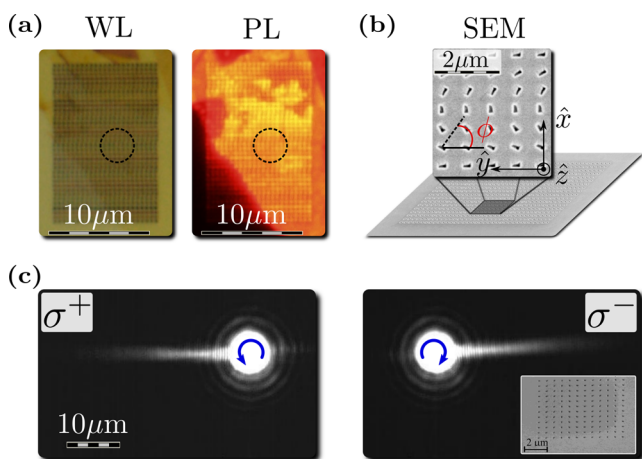


Figure 2. (a) White light (WL) microscope image of the sample and photoluminescence (PL) image of the same area under laser excitation at 2.58 eV. (b) SEM image of the plasmonic OSO resonator fabricated by sputtering 200 nm of gold on a glass substrate coated by a 5 nm thick chromium adhesion layer. The array with ϕ -rotated rectangular apertures is milled through the metallic layers using a focused ion beam (FIB). (c) Real-space leakage radiation microscope¹¹ images of the surface plasmons launched by σ⁺ and σ⁻ excitations on a OSO plasmonic resonator similar to the one of panel (b). Note that in these images, the leakage signal is not analyzed in polarization.

orbital period $6 \times \Lambda$ sets a rotation vector $\mathbf{\Omega} = (\phi/\Lambda)\hat{z}$, which combines with the spin σ of the incident light into a geometric phase $\Phi_g = -\Omega\sigma x$.³⁸ The gradient of this geometric phase imparts a momentum $\mathbf{k}_g = -\sigma(\phi/\Lambda)\hat{x}$ added to the matching condition on the array between the plasmonic \mathbf{k}_{SP} and incidence in-plane \mathbf{k}_{in} momenta: $\mathbf{k}_{SP} = \mathbf{k}_{in} + (2\pi/\Lambda)(n\hat{x} + m\hat{y}) + \mathbf{k}_g$. This condition defines different (*n*,*m*) orders for the plasmonic dispersions, which are transverse magnetic (TM) and transverse electric (TE) polarized along the *x* and *y* axis of the array, respectively (see Figure 2b). The dispersive properties of such a resonator thus combines two modal responses: plasmon excitations directly determined on the square Bravais lattice of the grating for both σ⁺ and σ⁻ illuminations via $(2\pi/\Lambda)(n\hat{x} + m\hat{y})$, and spin-dependent plasmon OSO modes launched by the additional geometric momentum \mathbf{k}_g . It is important to note that the contribution of the geometric phase impacts the TM dispersions only. The period of our structure $\Lambda = 480$ nm is optimized to have *n* = +1 and *n* = -1 TM modes resonant with the absorption energy of the A-exciton of WS₂ at 2.01 eV for σ⁺ and σ⁻ illuminations, respectively. This strict relation between *n* = ±1 and σ = ±1 is the OSO mechanism that breaks the left vs right symmetry of the modal response of the array, which in this sense becomes chiral. Plasmon OSO modes are, thus, launched in counter-propagating directions along the *x*-axis for opposite spins σ of the excitation light. In the case of a bare plasmonic OSO resonator, this is clearly observed in Figure 2c. We stress that similar arrangements of anisotropic apertures have previously been demonstrated to allow for spin-dependent surface plasmon launching.^{8,11,39,40}

As explained in the Supporting Information (section A), the low transmission measured through our WS₂/plasmonic array sample (Figure 2a) enables us to obtain absorption spectra directly from reflectivity spectra. Angle-resolved white light absorption spectra are hence recorded and shown in Figure 3a,b for left and right circular polarizations; see also the

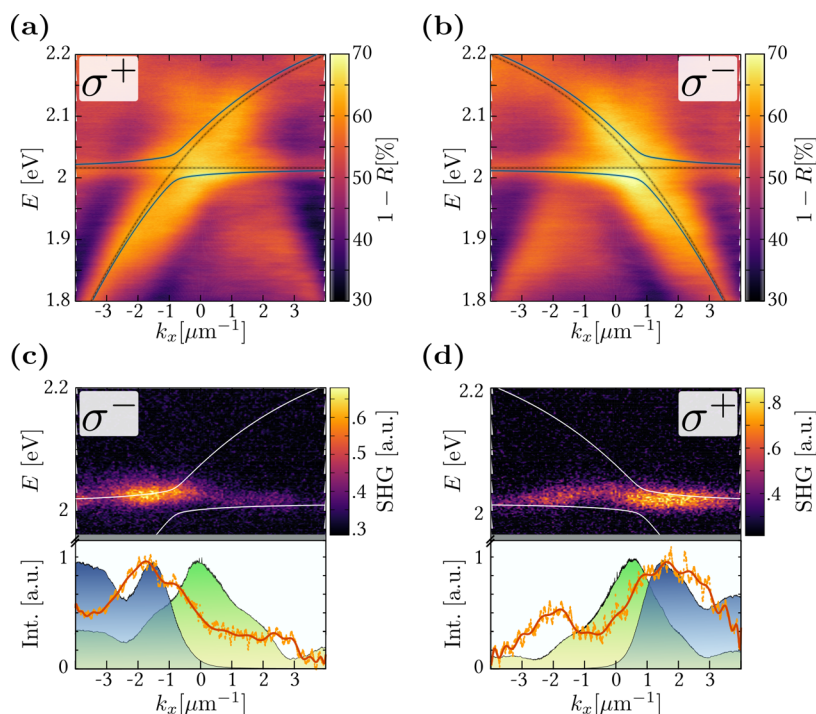


Figure 3. Angle-resolved absorption spectrum of the sample analyzed in (a) left and (b) right circular polarizations, with the best fit coupled oscillator model drawn. The horizontal dotted line corresponds to the uncoupled exciton energy 2.01 eV obtained from an absorption measurement away from the plasmonic resonator, while the dispersive dotted line corresponds to the OSO mode of the resonator, calculated from the dispersion relation given above. Angle-resolved resonant second harmonic spectrum for (c) right and (d) left circular excitations at 1.01 eV. These spectra have been recorded using a downconverted pulsed laser (120 fs, 1 kHz) focused to a diffraction-limited spot on the sample with a microscope objective (40 \times , NA = 0.6). Working in epi-configuration, the second harmonic signal is collected through the same objective. Corresponding crosscuts are displayed with the angular profile of the second harmonic signal (red curves), of the absorption spectra at 2.02 eV (green shades) and of the product (blue shades) between the absorption and the 4th power of the excitonic Hopfield coefficient of the chiralitonic state; see details in the [Supporting Information \(section D\)](#).

[Supporting Information \(section A\)](#) for the raw data. In each case, two strongly dispersing branches are observed, corresponding to upper and lower chiralitonic states. As detailed in the [Supporting Information \(section A\)](#), a fit of a coupled dissipative oscillators model to the dispersions enables us to extract a branch splitting $\sqrt{(\hbar\Omega_R)^2 - (\hbar\gamma_{\text{exc}} - \hbar\Gamma_{\text{OSO}})^2}/4 = 40$ meV at the crossing point at 2.01 eV between the uncoupled exciton and the OSO mode of the resonator. With measured line widths (full-width at half-maximum) of the excitonic mode $\hbar\gamma_{\text{exc}} = 26$ meV and of the plasmonic mode $\hbar\Gamma_{\text{OSO}} = 80$ meV, this fitting yields a Rabi frequency of $\hbar\Omega_R = 48$ meV, close to our previous observations on non-OSO plasmonic resonators.³³ We emphasize that this value gives a figure-of-merit $C = \Omega_R/(\gamma_{\text{exc}}/2 + \Gamma_{\text{OSO}}/2) = 0.9$ very close to the strong coupling $C = 1$ criterion.^{41,42} The fact that our system apparently remains at the onset of strong coupling through this criterion is only due (i) to spatial and spectral disorders and (ii) to the fact that an uncoupled Bravais plasmonic branch is always superimposed to the plasmonic OSO mode. Disorder leaves, as always for collective systems,⁴³ an inhomogeneous band of uncoupled states at the excitonic energy, while modal superimposition lead to asymmetric lineshapes clearly seen in [Figure 3a,b](#). These effects yield a relatively low level of visibility of the anticrossing which however can be better resolved through the first-derivative analysis of our absorption spectra shown in the [Supporting Information \(section A\)](#).

In such coupling conditions, the two dispersion diagrams also show a clear mirror symmetry breaking with respect to the normal incident axis ($k_x = 0$) for the two opposite optical spins. This clearly demonstrates the capability of our structure to act as a spin-momentum locked polariton launcher. From the extracted line width that gives the lifetime of the chiralitonic mode and the curvature of the dispersion relation that provides its group velocity, we can estimate a chiraliton propagation length of the order of 4 μm , in good agreement with the measured PL diffusion length presented in the [Supporting Information \(section B\)](#).

In view of chiral light–chiral matter interactions, it turns out to be particularly interesting to complement linear absorption spectroscopy with a look at the resonant second harmonic (SH) response of the coupled system. Indeed, resonant SH spectroscopy yields distinctive dispersive features which provide further evidence on the nature of the exciton-OSO mode coupling and the advent of chiralitonic states. Monolayer TMDs are known to give a high valley contrast in the generation of a SH signal resonant with their A-excitons,⁴⁴ as we also report in the [Supporting Information \(section C\)](#) for a bare WS₂ monolayer excited by a laser pump at $\omega = 1.01$ eV. The resonant SH signal writes as^{45,46}

$$I(2\omega) \propto (\rho_\omega I_\omega)^2 \cdot |\chi^{(2)}(2\omega)|^2 \cdot \rho_{2\omega} \quad (1)$$

where I_ω is the pump intensity, $\chi^{(2)}(2\omega)$ is the second order susceptibility associated with the coupled system, ρ_ω is the optical mode density of the resonator related to the fraction of

the pump intensity that reaches WS_2 , and $\rho_{2\omega}$ is the optical mode density of the resonator that determines the fraction of SH intensity decoupled into the far field at $2\hbar\omega = 2.02$ eV.

Under the same approximations of ref 47, the resonant second order susceptibility can be written as

$$\chi^{(2)}(2\omega) = \alpha^{(1)}(2\omega) \sum_n \frac{K_{eng}}{\omega_{ng} - \omega} \quad (2)$$

where \sum_n sums over virtual electronic transitions, and $K_{eng} = \langle e| \mathbf{p}|g \rangle \otimes \langle e| \mathbf{p}|n \rangle \otimes \langle n| \mathbf{p}|g \rangle$ is a third-rank tensor built on the electronic dipole moments \mathbf{p} taken between the excited e , virtual n , and ground g states. The prefactor $\alpha^{(1)}(2\omega)$ is the linear polarizability of the system at frequency 2ω , giving resonantly enhanced SH signal at every allowed $|g\rangle \rightarrow |e\rangle$ electronic transitions.

When the excited state is an uncoupled exciton associated with a transition energy fixed at frequency $2\hbar\omega = 2.01$ eV for all angles within the bandwidth of our pumping laser at 1.01 eV, the tensor K_{eng} is nondispersive. While ρ_{ω} can safely be assumed to be nondispersive at $\hbar\omega = 1.01$ eV, the angular distribution of the SH signal can only come from the dispersive nature of the resonator with $\rho_{2\omega}$ strongly dependent on the in-plane wave vector k_x . The optical mode density being proportional to the absorption, $\rho_{2\omega}(k_x)$ is given by the angular absorption spectrum shown in Figure 3a,b crosscut at $2\hbar\omega = 2.02$ eV and is plotted in the lower panels of Figure 3c,d. The SH signal related to the uncoupled (or weakly coupled) excitons is thus observed over the anticrossing region.

One however clearly sees on the angular features of the SH signals shown in Figure 3c,d an additional contribution shifted from the anticrossing region. Our interpretation is that this contribution stems from strongly coupled excitons. With two populations of uncoupled and strongly coupled WS_2 excitons, the SH signal is indeed expected to be resonantly enhanced when the SH frequency matches the transition frequency of either uncoupled or strongly coupled excitons.

The central point is that the contribution of strongly coupled exciton to the SH signal is determined by a dispersive resonant second order susceptibility $\chi^{(2)}(2\omega, k_x)$, in contrast with uncoupled excitons. This is expected because, if the excited state involved in the electronic transition $|g\rangle \rightarrow |e\rangle$ is a polaritonic state, the tensor K_{eng} must incorporate the associated excitonic Hopfield coefficient which is dispersive. This Hopfield coefficient $\beta_{\lambda}^j(k_x)$, defined in both $\lambda = K(K')$ valleys, is either the one associated with the upper $j = +$ or lower $j = -$ polaritonic state. In our framework, the pump at 1.01 eV can resonantly excite the upper polaritonic state; see Figure 1c. In such a case, with $|e\rangle \equiv |P_{K(K'),\sigma^{\pm}, \mp k_{SP}}^+\rangle$, the K_{eng} tensor is proportional to the excitonic Hopfield coefficient $[\beta_{K(K'),\sigma^{\pm}}^+(k_x)]^2$ evaluated by the procedure described in details Supporting Information (section A). Remarkably, as seen in the lower panels of Figure 3c,d, the angular distribution of the SH signal turns out following the product between the optical mode density $\rho_{2\omega}(k_x)$ and $|\chi^{(2)}(2\omega, k_x)|^2 \propto [\beta_{K(K'),\sigma^{\pm}}^+(k_x)]^4$ rather than $\rho_{2\omega}(k_x)$ only. Because it reveals the dispersive influence of $\beta_{K(K'),\sigma^{\pm}}^+(k_x)$, we interpret this clear deviation of the SH signal from the uncoupled contribution as the signature of the chiralitonic states.

The resonant SH spectroscopy also confirms that the valley contrast of WS_2 and the spin-locking property of the OSO

plasmonic resonator are imprinted on these new coupled states of the system. This is seen by observing in Figure 3c,d the angular exchange of the SH signals when the spin of the excitation is reversed from right to left circular polarization. The right versus left contrast (ca. 20%) close to the one measured on the reflectivity maps (ca. 15%) demonstrates the selective coupling of excitons in one valley to surface plasmons propagating in one direction, thus, realizing valley-contrasting chiralitonic states with spins locked to their propagation wavevectors:

$$\begin{aligned} |P_{K',\sigma^+, -k_{SP}}^{\pm}\rangle &= |g_{K'}, 1_{\sigma^+}, -k_{SP}\rangle \pm |e_{K'}, 0_{\sigma^+}, -k_{SP}\rangle \\ |P_{K',\sigma^-, +k_{SP}}^{\pm}\rangle &= |g_{K'}, 1_{\sigma^-}, +k_{SP}\rangle \pm |e_{K'}, 0_{\sigma^-}, +k_{SP}\rangle \end{aligned}$$

where $e_i(g_i)$ corresponds to the presence (absence) of an exciton in the valley $i = (K, K')$ of WS_2 , and $1_j(0_j)$ to $1(0)$ plasmon in the mode of polarization $j = (\sigma^+, \sigma^-)$ and wavevector $\pm k_{SP}$.

Revealed by these resonant SH measurements, the spin-locking property of chiralitonic states incurs however different relaxation mechanisms through the dynamical evolution of the chiralitons. In particular, excitonic intervalley scattering can erase valley contrast in WS_2 at RT,⁴⁸ see below. In our configuration, this would transfer chiraliton population from one valley to the other, generating via optical spin-locking, a reverse flow, racemizing the chiraliton population. This picture however does not account for the possibility of more robust valley contrasts in strong coupling conditions, as recently reported with $MoSe_2$ in Fabry-Pérot cavities.²⁵ The chiralitonic flow is measured by performing angle resolved polarized PL experiments, averaging the signal over the PL lifetime of about 200 ps (see Supporting Information, sections D and E). For these experiments, the laser excitation energy is chosen at 1.96 eV, slightly below the WS_2 band gap. At this energy, the measured PL results from a phonon-induced up-conversion process that minimizes intervalley scattering events.⁴⁹ The difference between PL dispersions obtained with left and right circularly polarized excitations is displayed in Figure 4a, showing net flows of chiralitons with spin-determined momenta. This is in agreement with the differential white-light reflectivity map $R_{\sigma^-} - R_{\sigma^+}$ of Figure 4b. Considering that this map gives the sorting efficiency of our OSO resonator, such correlations in the PL imply that the effect of the initial spin-momentum determination of the chiralitons (see Figure 3e,f) is still observed after 200 ps at RT. After this PL lifetime, a net chiral flow $\mathcal{F} = I_{\sigma^-} - I_{\sigma^+}$ of $\sim 6\%$ is extracted from Figure 4a. This is the signature of a chiralitonic valley polarization, in striking contrast with the absence of valley polarization that we report for a bare WS_2 monolayer at RT in the Supporting Information, section G. The extracted net flow is however limited by the finite optical contrast C of our OSO resonator, which we measure at a 15% level from a cross-cut taken on Figure 4b at 1.98 eV. It is therefore possible to infer that a chiralitonic valley contrast of $\mathcal{F}/C \simeq 40\%$ can be reached at RT for the strongly coupled WS_2 monolayer. We understand this surprisingly robust contrast by invoking the fact that selectively coupling the K/K' valley exciton of the TMD to the particular $\mp k_{SP}$ OSO mode offers a new possibility to bypass the valley relaxation and decoherence processes. Moreover from the polaritonic point of view, the local dephasing and scattering processes at play on bare excitons, that erase valley

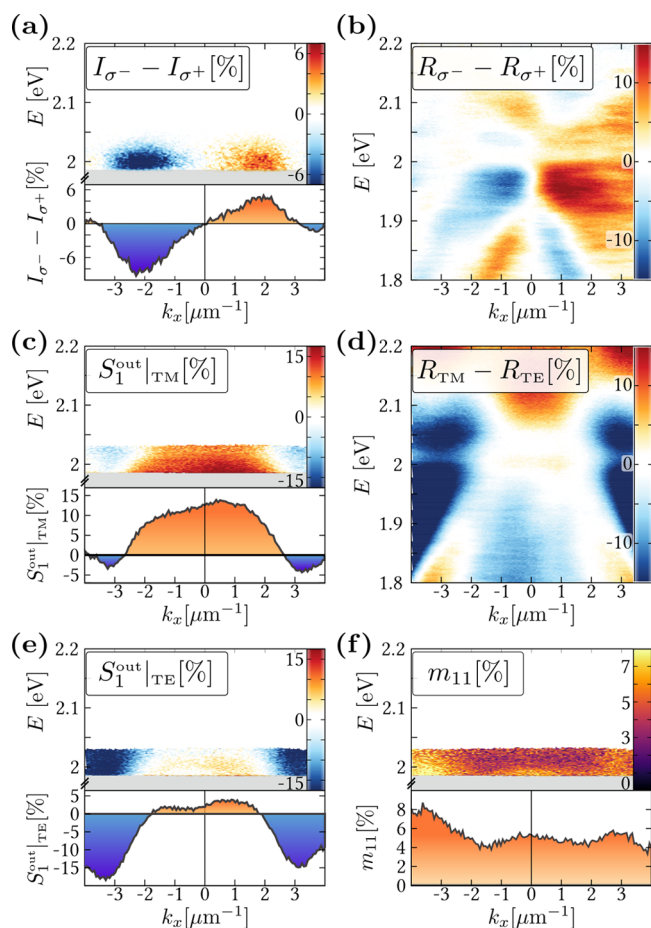


Figure 4. (a) Differential PL dispersion spectrum for left and right circularly polarized excitations. The shaded regions in all panels are removed by the laser line filter, and the cross-cuts are taken at 2 eV. (b) Differential angle-resolved reflection spectrum for left and right circularly polarized light. (c), (e) Angle-resolved spectrum of the normalized coefficient $S_1^{\text{out}}|_{\text{TM(TE)}}/S_0$ of the PL Stokes vector for a TM(TE) polarized excitation (see text for details). Note that we have put a detection threshold below 100 photon counts that cuts the signal above ~ 2.03 eV in panels (a), (c), (e), and (f). (d) Differential angle-resolved reflection spectrum obtained from analyzed TM and TE measurements. (f) k_x -energy dispersion of the degree of chiralitonic intervalley coherence m_{11} computed from (c) and (e). The asymmetry observed in the m_{11} profile can be traced back to the differential coupling efficiencies of the OSO resonator for left and right polarizations. Such differential efficiencies, clearly seen in Figure 3, stem from imperfections in the focused ion beam lithography of the array.

contrasts on a bare WS_2 flake, as observed in the Supporting Information, section F, are reduced by the delocalized nature of the chiralitonic state, a process akin to motional narrowing and recently observed on other polaritonic systems.^{26,28,50} This being said, it is clear that further theoretical work is needed in order to understand how the tagging of a polaritonic state by the in-plane momentum of the plasmonic OSO mode can lead to such a protection. Nevertheless, this investigation goes beyond the scope of the present work.

As a consequence of these protection mechanisms, such a coupled system involving atomically thin crystals of TMDs can provide new ways to incorporate intervalley coherent dynamics^{22,24,51–53} into the realm of polariton physics. To illustrate this, we now show that two counter-propagating flows

of chiralitons can evolve coherently. It is clear from Figure 1c that within such a coherent superposition of counter-propagating chiralitons

$$|\Psi\rangle = |P_{K,\sigma^+,-k_{\text{sp}}}\rangle + |P_{K',\sigma^-,+k_{\text{sp}}}\rangle \quad (3)$$

flow directions and spin polarizations become nonseparable. Intervalley coherence is expected to result in a nonzero degree of linearly polarized PL when excited by the same linear polarization chosen either vertical V or horizontal H. Functioning as a diffraction grating, the resonator encodes these linear polarization respectively into TM (V) and TE (H) modes; for more details, see Supporting Information (section G). This can be monitored by measuring the $S_1 = I_{\text{TM}} - I_{\text{TE}}$ coefficient of the PL Stokes vector, where $I_{\text{TM(TE)}}$ is the emitted PL intensity analyzed in TM (TE) polarization. This coefficient is displayed in the k_x -energy plane in Figure 4c for an incident TM polarized excitation at 1.96 eV. Note that negative value regions in $S_1^{\text{out}}|_{\text{TM}}$ only show that the part of the chiralitonic population that lost intervalley coherence is dominating the total PL in the region of the dispersion where the TE mode dominates over the TM mode. Figure 4e displays the same coefficient under TE excitation, hence an analogous discussion related this time to positive values of the $S_1^{\text{out}}|_{\text{TE}}$. A clear polarization anisotropy on the chiraliton emission is observed for both TM and TE excitation polarizations, both featuring the same symmetry along the $k_x = 0$ axis as the differential reflectivity dispersion map $R_{\text{TM}} - R_{\text{TE}}$ shown in Figure 4d. As detailed in the Supporting Information (section G), the degree of chiralitonic intervalley coherence can be directly quantified by the difference $(S_1^{\text{out}}|_{\text{TM}} - S_1^{\text{out}}|_{\text{TE}})/2$, which measures the PL linear depolarization factor displayed (as m_{11}) in Figure 4f. By this procedure, we retrieve a chiralitonic intervalley coherence that varies between 5% and 8% depending on k_x . Interestingly, these values that we reach at RT have magnitudes comparable to those reported on a bare WS_2 monolayer at 10 K.⁵⁴ This unambiguously shows how such coupled TMD-OSO systems can sustain RT coherent dynamics that are robust enough to be observed over the plasmonic propagation distances despite the long exciton PL lifetimes.

In summary, we demonstrate valley contrasting spin-momentum locked chiralitonic states in an atomically thin TMD semiconductor coupled to a plasmonic OSO resonator. Surprisingly, while the bare exciton does not display any, we observe clear RT valley contrasts and coherences on our coupled system, that persist even after 200 ps lifetimes. This leads to the possibility of exploiting such robust coherences and measure chiralitonic flows that can evolve in superpositions over micron scale distances. Our results show that the combination of OSO interactions with TMD valleytronics is an interesting path to follow in order to explore and manipulate RT coherences in chiral quantum architectures.^{20,55}

■ ASSOCIATED CONTENT

📄 Supporting Information

The Supporting Information is available free of charge on the ACS Publications website at DOI: 10.1021/acsphtons.7b01032.

Section A. Linear absorption dispersion analysis: details the first derivative absorption spectra and the coupled oscillator fits from which the strong coupling criterion is derived. Section B. Chiraliton diffusion length: presents the measurements of the 1/e decay length of the

polaritonic states. Section C. Resonant second harmonic generation on a WS monolayer: displays the valley contrasted resonant second harmonic spectra. Section D. PL lifetime measurement on the coupled system: shows the results of Time-Correlated Single Photon Counting under picosecond pulsed excitation of the WS monolayer. Section E. Optical setup: presents the setup used for the angle-resolved polarimetric measurements. Section F. Valley contrast measurements on a bare WS monolayer: reports the absence of valley contrasts measured at room temperature on a bare monolayer. Section G. Angle-resolved Stokes vector polarimetry: details the polarimetric approach implemented for characterizing the polarization state of the chiraliton and the degree of intervalley coherence (PDF).

AUTHOR INFORMATION

Corresponding Author

*E-mail: genet@unistra.fr.

ORCID

Stéphane Bercaud: 0000-0002-5753-3671

Thomas W. Ebbesen: 0000-0002-3999-1636

Cyriaque Genet: 0000-0003-0672-7406

Author Contributions

[‡]These authors contributed equally to this work.

Notes

The authors declare no competing financial interest.

ACKNOWLEDGMENTS

We thank David Hagenmüller for fruitful discussions. This work was supported in part by the ANR Equipex “Union” (ANR-10-EQPX-52-01), ANR Grant (H2DH ANR-15-CE24-0016), the Labex NIE projects (ANR-11-LABX-0058-NIE), and USIAS within the Investissement d’Avenir program ANR-10-IDEX-0002-02. Y.G. acknowledges support from the Ministry of Science, Technology and Space, Israel. C.G. and Y.G. acknowledge additional support from the French CNRS and the Israeli MOST through a PICS-PRC grant. S.B. is a member of the Institut Universitaire de France (IUF).

REFERENCES

- (1) Bliokh, K. Y.; Rodríguez-Fortuño, F.; Nori, F.; Zayats, A. V. Spin-orbit interactions of light. *Nat. Photonics* **2015**, *9*, 796–808.
- (2) Bomzon, Z.; Biener, G.; Kleiner, V.; Hasman, E. Space-variant Pancharatnam–Berry phase optical elements with computer-generated subwavelength gratings. *Opt. Lett.* **2002**, *27*, 1141–1143.
- (3) Le Feber, B.; Rotenberg, N.; Kuipers, L. Nanophotonic control of circular dipole emission. *Nat. Commun.* **2015**, *6*, 6695.
- (4) Petersen, J.; Volz, J.; Rauschenbeutel, A. Chiral nanophotonic waveguide interface based on spin-orbit interaction of light. *Science* **2014**, *346*, 67–71.
- (5) Rafayelyan, M.; Tkachenko, G.; Brasselet, E. Reflective spin-orbit geometric phase from chiral anisotropic optical media. *Phys. Rev. Lett.* **2016**, *116*, 253902.
- (6) Bliokh, K. Y.; Gorodetski, Y.; Kleiner, V.; Hasman, E. Coriolis effect in optics: unified geometric phase and spin-Hall effect. *Phys. Rev. Lett.* **2008**, *101*, 030404.
- (7) Gorodetski, Y.; Drezet, A.; Genet, C.; Ebbesen, T. W. Generating far-field orbital angular momenta from near-field optical chirality. *Phys. Rev. Lett.* **2013**, *110*, 203906.
- (8) Lin, J.; Mueller, J. B.; Wang, Q.; Yuan, G.; Antoniou, N.; Yuan, X.-C.; Capasso, F. Polarization-controlled tunable directional coupling of surface plasmon polaritons. *Science* **2013**, *340*, 331–334.
- (9) Rodríguez-Fortuño, F. J.; Marino, G.; Ginzburg, P.; O’Connor, D.; Martínez, A.; Wurtz, G. A.; Zayats, A. V. Near-Field Interference for the Unidirectional Excitation of Electromagnetic Guided Modes. *Science* **2013**, *340*, 328–330.
- (10) Spektor, G.; David, A.; Gjonaj, B.; Bartal, G.; Orenstein, M. Metafocusing by a metasprial plasmonic lens. *Nano Lett.* **2015**, *15*, 5739–5743.
- (11) Jiang, Q.; Pham, A.; Berthel, M.; Huant, S.; Bellessa, J.; Genet, C.; Drezet, A. Directional and Singular Surface Plasmon Generation in Chiral and Achiral Nanostructures Demonstrated by Leakage Radiation Microscopy. *ACS Photonics* **2016**, *3*, 1116–1124.
- (12) O’Connor, D.; Ginzburg, P.; Rodríguez-Fortuño, F. J.; Wurtz, G. A.; Zayats, A. V. Spin-orbit coupling in surface plasmon scattering by nanostructures. *Nat. Commun.* **2014**, *5*, 5327.
- (13) Mitsch, R.; Sayrin, C.; Albrecht, B.; Schneeweiss, P.; Rauschenbeutel, A. Quantum state-controlled directional spontaneous emission of photons into a nanophotonic waveguide. *Nat. Commun.* **2014**, *5*, 5713.
- (14) Junge, C.; O’Shea, D.; Volz, J.; Rauschenbeutel, A. Strong Coupling between Single Atoms and Nontransversal Photons. *Phys. Rev. Lett.* **2013**, *110*, 213604.
- (15) Söllner, I.; Mahmoodian, S.; Hansen, S. L.; Midolo, L.; Javadi, A.; Kiršanskė, G.; Pregnolato, T.; El-Ella, H.; Lee, E. H.; Song, J. D.; Stobbe, S.; Lodahl, P. Deterministic photon-emitter coupling in chiral photonic circuits. *Nat. Nanotechnol.* **2015**, *10*, 775–778.
- (16) Gonzalez-Ballester, C.; Gonzalez-Tudela, A.; Garcia-Vidal, F. J.; Moreno, E. Chiral route to spontaneous entanglement generation. *Phys. Rev. B: Condens. Matter Mater. Phys.* **2015**, *92*, 155304.
- (17) Sayrin, C.; Junge, C.; Mitsch, R.; Albrecht, B.; O’Shea, D.; Schneeweiss, P.; Volz, J.; Rauschenbeutel, A. Nanophotonic Optical Isolator Controlled by the Internal State of Cold Atoms. *Phys. Rev. X* **2015**, *5*, 041036.
- (18) Young, A. B.; Thijssen, A. C. T.; Beggs, D. M.; Androvitsaneas, P.; Kuipers, L.; Rarity, J. G.; Hughes, S.; Oulton, R. Polarization engineering in photonic crystal waveguides for spin-photon entanglers. *Phys. Rev. Lett.* **2015**, *115*, 153901.
- (19) Gonzalez-Ballester, C.; Moreno, E.; Garcia-Vidal, F. J.; Gonzalez-Tudela, A. Nonreciprocal few-photons routing schemes based on chiral waveguide-emitter couplings. *Phys. Rev. A: At., Mol., Opt. Phys.* **2016**, *94*, 063817.
- (20) Coles, R. J.; Price, D. M.; Dixon, J. E.; Royall, B.; Clarke, E.; Kok, P.; Skolnick, M. S.; Fox, A. M.; Makhonin, M. N. Chirality of nanophotonic waveguide with embedded quantum emitter for unidirectional spin transfer. *Nat. Commun.* **2016**, *7*, 11183.
- (21) Lodahl, P.; Mahmoodian, S.; Stobbe, S.; Schneeweiss, P.; Volz, J.; Rauschenbeutel, A.; Pichler, H.; Zoller, P. Chiral Quantum Optics. *Nature* **2017**, *541*, 473–480.
- (22) Jones, A. M.; Yu, H.; Ghimire, N. J.; Wu, S.; Aivazian, G.; Ross, J. S.; Zhao, B.; Yan, J.; Mandrus, D. G.; Xiao, D.; Yao, W.; Xu, X. Optical generation of excitonic valley coherence in monolayer WSe₂. *Nat. Nanotechnol.* **2013**, *8*, 634–638.
- (23) Moody, G.; Schaibley, J.; Xu, X. Exciton dynamics in monolayer transition metal dichalcogenides. *J. Opt. Soc. Am. B* **2016**, *33*, C39–C49.
- (24) Hao, K.; Moody, G.; Wu, F.; Dass, C. K.; Xu, L.; Chen, C.-H.; Sun, L.; Li, M.-Y.; Li, L.-J.; MacDonald, A. H.; Li, X. Direct measurement of exciton valley coherence in monolayer WSe₂. *Nat. Phys.* **2016**, *12*, 677.
- (25) Dufferwiel, S.; Lyons, T. P.; Solnyshkov, D. D.; Trichet, A. A. P.; Withers, F.; Schwarz, S.; Malpuech, G.; Smith, J. M.; Novoselov, K. S.; Skolnick, M. S.; Krizhanovskii, D. N.; Tartakovskii, A. I. Valley addressable exciton-polaritons in atomically thin semiconductors. *Nat. Photonics* **2017**, *11*, 497–501.
- (26) Chen, Y.-J.; Cain, J. D.; Stanev, T. K.; Dravid, V. P.; Stern, N. P. Valley-Polarized Exciton-Polaritons in a Monolayer Semiconductor. *Nat. Photonics* **2017**, *11*, 431–435.
- (27) Sun, Z.; Gu, J.; Ghazaryan, A.; Shotan, Z.; Considine, C. R.; Dollar, M.; Chakraborty, B.; Liu, X.; Ghaemi, P.; Kéna-Cohen, S.;

Menon, V. M. Optical control of room-temperature valley polaritons. *Nat. Photonics* **2017**, *11*, 491–496.

(28) Kleemann, M.-E.; Chikkaraddy, R.; Alexeev, E. M.; Kos, D.; Carnegie, C.; Deacon, W.; de Casalis de Pury, A.; Grosse, C.; de Nijs, B.; Mertens, J.; Tartakovskii, A. I.; Baumberg, J. J. Strong-coupling of WSe₂ in ultra-compact plasmonic nanocavities at room temperature. *Nat. Commun.* **2017**, *8*, 1296.

(29) Liu, X.; Galfsky, T.; Sun, Z.; Xia, F.; Lin, E.-C.; Lee, Y.-H.; Kéna-Cohen, S.; Menon, V. M. Strong light-matter coupling in two-dimensional atomic crystals. *Nat. Photonics* **2015**, *9*, 30–34.

(30) Dufferwiel, S.; et al. Exciton-polaritons in van der Waals heterostructures embedded in tunable microcavities. *Nat. Commun.* **2015**, *6*, 8579.

(31) Sidler, M.; Back, P.; Cotlet, O.; Srivastava, A.; Fink, T.; Kroner, M.; Demler, E. Fermi polaron-polaritons in charge-tunable atomically thin semiconductors. *Nat. Phys.* **2016**, *13*, 255–261.

(32) Liu, W.; Lee, B.; Naylor, C. H.; Ee, H.-S.; Park, J.; Johnson, A. T. C.; Agarwal, R. Strong Exciton-Plasmon Coupling in MoS₂ Coupled with Plasmonic Lattice. *Nano Lett.* **2016**, *16*, 1262–1269.

(33) Wang, S.; Li, S.; Chervy, T.; Shalabney, A.; Azzini, S.; Orgiu, E.; Hutchison, J. A.; Genet, C.; Samorì, P.; Ebbesen, T. W. Coherent Coupling of WS₂ Monolayers with Metallic Photonic Nanostructures at Room Temperature. *Nano Lett.* **2016**, *16*, 4368–4374.

(34) Li, Y.; Chernikov, A.; Zhang, X.; Rigosi, A.; Hill, H. M.; van der Zande, A. M.; Chenet, D. A.; Shih, E.-M.; Hone, J.; Heinz, T. F. Measurement of the optical dielectric function of monolayer transition-metal dichalcogenides: MoS₂, MoSe₂, WS₂, and WSe₂. *Phys. Rev. B: Condens. Matter Mater. Phys.* **2014**, *90*, 205422.

(35) Mak, K. F.; Shan, J. Photonics and optoelectronics of 2D semiconductor transition metal dichalcogenides. *Nat. Photonics* **2016**, *10*, 216–226.

(36) Li, Z.; Li, Y.; Han, T.; Wang, X.; Yu, Y.; Tay, B.; Liu, Z.; Fang, Z. Tailoring MoS₂ Exciton Plasmon Interaction by Optical Spin Orbit Coupling. *ACS Nano* **2017**, *11*, 1165–1171.

(37) Gong, S.-H.; Alpegiani, F.; Sciacca, B.; Garnett, E. C.; Kuipers, L. Nanoscale chiral valley-photon interface through optical spin-orbit coupling. *Science* **2017**, *359*, 443.

(38) Bliokh, K. Y.; Gorodetski, Y.; Kleiner, V.; Hasman, E. Coriolis effect in optics: unified geometric phase and spin-Hall effect. *Phys. Rev. Lett.* **2008**, *101*, 030404.

(39) Shitrit, N.; Bretner, I.; Gorodetski, Y.; Kleiner, V.; Hasman, E. Optical Spin Hall Effects in Plasmonic Chains. *Nano Lett.* **2011**, *11*, 2038–2042.

(40) Huang, L.; Chen, X.; Bai, B.; Tan, Q.; Jin, G.; Zentgraf, T.; Zhang, S. Helicity dependent directional surface plasmon polariton excitation using a metasurface with interfacial phase discontinuity. *Light: Sci. Appl.* **2013**, *2*, e70.

(41) Houdré, R. Early stages of continuous wave experiments on cavity-polaritons. *Phys. Status Solidi B* **2005**, *242*, 2167–2196.

(42) Törmä, P.; Barnes, W. L. Strong coupling between surface plasmon polaritons and emitters: a review. *Rep. Prog. Phys.* **2015**, *78*, 013901.

(43) Canaguier-Durand, A.; Devaux, E.; George, J.; Pang, Y.; Hutchison, J. A.; Schwartz, T.; Genet, C.; Wilhelms, N.; Lehn, J.-M.; Ebbesen, T. W. Thermodynamics of Molecules Strongly Coupled to the Vacuum Field. *Angew. Chem.* **2013**, *125*, 10727–10730.

(44) Seyler, K. L.; Schaibley, J. R.; Gong, P.; Rivera, P.; Jones, A. M.; Wu, S.; Yan, J.; Mandrus, D. G.; Yao, W.; Xu, X. Electrical control of second-harmonic generation in a WSe₂ monolayer transistor. *Nat. Nanotechnol.* **2015**, *10*, 407–411.

(45) Heinz, T. F.; Chen, C. K.; Ricard, D.; Shen, Y. R. Spectroscopy of Molecular Monolayers by Resonant Second-Harmonic Generation. *Phys. Rev. Lett.* **1982**, *48*, 478–481.

(46) Chervy, T.; Xu, J.; Duan, Y.; Wang, C.; Mager, L.; Frerejean, M.; Munninghoff, J. A.; Tinnemans, P.; Hutchison, J. A.; Genet, C.; Rowan, A.; Rasing, T.; Ebbesen, T. W. High-Efficiency Second-Harmonic Generation from Hybrid Light-Matter States. *Nano Lett.* **2016**, *16*, 7352–7356.

(47) Lin, S. H.; Alden, R. G.; Villaeys, A. A.; Pflumio, V. Theory of second-harmonic generation of molecular systems: The steady-state case. *Phys. Rev. A: At., Mol., Opt. Phys.* **1993**, *48*, 3137–3151.

(48) Hanbicki, A. T.; McCreary, K. M.; Kioseoglou, G.; Currie, M.; Hellberg, C. S.; Friedman, A. L.; Jonker, B. T. High room temperature optical polarization due to spin-valley coupling in monolayer WS₂. *AIP Adv.* **2016**, *6*, 055804.

(49) Jones, A. M.; Yu, H.; Schaibley, J. R.; Yan, J.; Mandrus, D. G.; Taniguchi, T.; Watanabe, K.; Dery, H.; Yao, W.; Xu, X. Excitonic luminescence upconversion in a two-dimensional semiconductor. *Nat. Phys.* **2016**, *12*, 323–327.

(50) Whittaker, D. M.; Kinsler, P.; Fisher, T. A.; Skolnick, M. S.; Armitage, A.; Afshar, A. M.; Sturge, M. D.; Roberts, J. S. Motional Narrowing in Semiconductor Microcavities. *Phys. Rev. Lett.* **1996**, *77*, 4792–4795.

(51) Wang, G.; Marie, X.; Liu, B. L.; Amand, T.; Robert, C.; Cadiz, F.; Renucci, P.; Urbaszek, B. Control of Exciton Valley Coherence in Transition Metal Dichalcogenide Monolayers. *Phys. Rev. Lett.* **2016**, *117*, 187401.

(52) Schmidt, R.; Arora, A.; Plechinger, G.; Nagler, P.; Granados del Aguila, A.; Ballottin, M. V.; Christianen, P. C. M.; Michaelis de Vasconcellos, S.; Schuller, C.; Korn, T.; Bratschitsch, R. Magnetic-field induced rotation of polarized emission from monolayer WS₂. *Phys. Rev. Lett.* **2016**, *117*, 077402.

(53) Ye, Z.; Sun, D.; Heinz, T. F. Optical manipulation of valley pseudospin. *Nat. Phys.* **2016**, *13*, 26–29.

(54) Zhu, B.; Zeng, H.; Dai, J.; Gong, Z.; Cui, X. Anomalously robust valley polarization and valley coherence in bilayer WS₂. *Proc. Natl. Acad. Sci. U. S. A.* **2014**, *111*, 11606–11611.

(55) Low, T.; Chaves, A.; Caldwell, J. D.; Kumar, A.; Fang, N. X.; Avouris, P.; Heinz, T. F.; Guinea, F.; Martin-Moreno, L.; Koppens, F. Polaritons in layered two-dimensional materials. *Nat. Mater.* **2017**, *16*, 182–194.